



**Metal Process Simulation Laboratory  
Department of Mechanical and Industrial Engineering  
University of Illinois at Urbana-Champaign  
Urbana, IL 61801**



# **Simple Model of Microsegregation during Solidification of Steels**

**Young-Mok Won  
Brian G. Thomas**

**Continuous Casting Consortium**

**REPORT**

**Submitted to**

**Allegheny Ludlum  
AK Steel  
Columbus Stainless  
ISPAT Inland Steel  
LTV  
Stollberg, Inc.**

**September 25, 2000**

# **Simple Model of Microsegregation during Solidification of Steels**

**Young-Mok Won and Brian G. Thomas**

University of Illinois at Urbana-Champaign  
Department of Mechanical and Industrial Engineering  
1206 W. Green Street, Urbana, IL 61801, U.S.A.

## Abstract

A simple analytical model of microsegregation for the solidification of multicomponent steel alloys is presented. This model is based on the Clyne-Kurz model and is extended to take into account the effects of multiple components, columnar dendrite microstructure, coarsening and the  $\delta/\gamma$  transformation. A new empirical equation to predict secondary dendrite arm spacing as a function of cooling rate and carbon content is presented based on experimental data measured by several different researchers. The simple microsegregation model is applied to predict phase fractions during solidification, microsegregation of solute elements, and the solidus temperature. The predictions agree well with a range of measured data and the results of a complete finite-difference model. The solidus temperature decreases with either increasing cooling rate or increasing secondary dendrite arm spacing. However, the secondary dendrite arm spacing during solidification decreases with increasing cooling rate. These two opposite effects partly cancel so the solidus temperature does not change much during solidification of a real casting.

KEY WORDS: microsegregation; solidification; multicomponent; solute element; Clyne-Kurz model; columnar dendrite; coarsening;  $\delta/\gamma$  peritectic transformation; secondary dendrite arm spacing; FDM model; steel; zero strength temperature; zero ductility temperature; cooling rate

## I. INTRODUCTION

Solidification phenomena play a major role in such diverse operations such as casting, crystal growth and welding. Solidification proceeds at various rates, which are sometimes far from equilibrium. Thus, the microstructure obtained is generally not homogeneous and gives rise to variations in composition with position at both small and large scales, which is known as segregation.

Solute segregation is important because it leads to non-equilibrium phases, cracks, and other problems, which lower the mechanical properties of the final product. Over the last three decades, attention has focused on segregation of aluminum and steel alloys, owing to their great commercial importance and susceptibility to this solidification problem. Segregation affects all processes, including foundry, ingot and continuous casting.

Segregation is classified according to its scale as: macrosegregation and microsegregation. Macroscopic segregation occurs on the scale of the grains or the entire casting and can be observed with the naked eye. It arises from large-scale fluid flow, caused by forced, natural and solutal convection. It requires the transport of solute-rich or -poor liquid and solid phases during solidification over distances much larger than the dendrite arm spacing. One unavoidable cause is the interdendritic flow of liquid due to solidification shrinkage and changes in the liquid density. These density changes can be caused by temperature changes or by changes in the liquid composition[1-3]. It is also affected by nozzles, which direct the liquid, electromagnetic forces, which enhance mixing[4-6], and by thermal or mechanical bulging or deformation of the casting during solidification[7]. Microsegregation refers to composition variation within the columnar

or equiaxed dendritic solidification structure, which has a length scale on the order of only a few micrometers. Clearly, macrosegregation prediction is very complex. Among many other things, it depends on an accurate prediction of microsegregation.

Microsegregation is caused by the redistribution of solute during solidification, as solute is generally rejected into the liquid[8]. Its fundamental cause is the difference between the thermodynamic equilibrium solubility of alloy elements in the different phases, which coexist in the mushy region during solidification. This is combined with the inability of solid-state diffusion to fully return the composition to its equilibrium constant level after solidification is complete, owing to the short times and small diffusion coefficients involved. Quantitative prediction of these phenomena is complicated by several difficulties:

- 1) quantifying the equilibrium solubility of each phase as a function of temperature. This is traditionally done using partition coefficients, which are reasonable for low concentrations, but requires the full multicomponent phase diagram for complex systems or higher alloy contents[9].
- 2) solving for diffusion transport within the solid phases, which requires a) knowledge of the diffusion coefficients for each element, b) the length scale, which depends on the solidifying microstructure and varies from the secondary to the primary dendrite arm spacing to the grain size, and c) the cooling conditions, which depend on macroscopic heat conduction in the casting.
- 3) linking of the microsegregation phenomena with the fluid flow and associated macrosegregation. This is complicated because flow occurs on at least three size scales, including flow within the interdendritic spaces, flow between grains, and flow in the bulk liquid[10].

4) accounting for phase transformations such as the peritectic transformation in steel, eutectic formation in aluminum alloys and precipitate formation.

The purpose of the present work is to develop, validate, and apply a fast and simple microsegregation model for the solidification of multicomponent steel alloys, which can be incorporated into other macroscopic models such as thermal-stress analysis. The solubility levels are based on liquidus temperatures and partition coefficients taken from available measurements for multicomponent steel alloys as are the diffusion coefficients. To obtain the microstructural length scales, an empirical equation is developed to quantify the secondary dendrite arm spacing as a function of carbon content and cooling rate, based on experimental measurements of the final microstructures. This is because microstructure prediction is a very difficult task which requires computationally intensive modeling methods such as phase field[11-16] and cellular automata[9,17-20]. The cooling history needed by the model is planned to be calculated by a separate model, so in the present work, the cooling rate is simply input to match experiments or treated as a parameter. Linking of the model with flow is ignored. This simple model of microsegregation also takes into account the effects of coarsening and the  $\delta/\gamma$  peritectic transformation.

To validate this simple microsegregation model, its predictions are compared with both relevant experimental measurements by previous researchers[17,21-30] and more accurate finite difference model calculations. Finally, the effects of cooling rate, secondary dendrite arm spacing and steel composition on microsegregation are investigated in a parametric study.

## II. PREVIOUS WORK

Many microsegregation models[8,10,17,18,31-38] with different assumptions and simplifications have been developed to predict solute redistribution and related phenomena. Numerous studies[8,31-34] on microsegregation models have been carried out for only binary alloys. Some studies[9,10,17-20,35-38] modeled microsegregation during solidification of steels taking into account binary[10,36], five[17-20] or more[9,37,38] solute elements and the peritectic reaction.

The heart of most simple microsegregation models is the assumed relationship between alloy concentration and solid fraction. This relationship can be evaluated to generate the one-dimensional composition profile between adjacent dendrite arms. These different relationships are now discussed, in order of increasing complexity.

The Lever rule model is an equilibrium solidification model, which assumes complete diffusion to equilibrium of all alloying elements in both the liquid and the solid phases as follows:

$$C_{L,i} = \frac{C_{o,i}}{f_S(k_i - 1) + 1} \quad (1)$$

where  $C_{L,i}$  is the liquid concentration of a given solute element at the solid-liquid interface,  $C_{o,i}$  is the initial liquid concentration,  $k_i$  is the equilibrium partition coefficient for that element and  $f_S$  is the solid fraction. The Lever rule model is usually inaccurate later during solidification,

because diffusion in the solid phases is too slow, especially for larger solute atoms such as manganese.

The opposite limiting case to the Lever rule model is the Scheil equation[31] or the “non-equilibrium Lever rule”. This model assumes no diffusion in the solid phase, complete diffusion in the liquid phase and local equilibrium at the solid-liquid interface as follows.

$$C_{L,i} = C_{o,i} (1 - f_S)^{k-1} \quad (2)$$

However, it is apparent that the Scheil equation does not adequately estimate the final solute concentration, because  $C_L$  becomes infinite at  $f_S = 1$ . This model is only useful for very rapid solidification processes, such as laser welding where the cooling rates exceed  $10^2$  °C/sec[21].

In order to predict microsegregation during steel solidification, finite non-zero diffusion must be considered at least in the solid phase. Many simple microsegregation models[32-34] have been proposed, which assume fixed dendrite arm spacing, constant physical properties in the solid phase, thermodynamic equilibrium at the solid-liquid interface, and straight liquidus or/and solidus lines in the equilibrium phase diagram[39-43]. Brody and Flemings[32] have proposed a general form of this model which assumes complete diffusion in the liquid phase and incomplete back-diffusion in the solid phase as follows

$$C_{L,i} = C_{o,i} [1 - (1 - \beta k_i) f_S]^{(k_i - 1)/(1 - \beta k_i)} \quad (3)$$



This general form introduces  $\beta$  as a back-diffusion parameter, which has been quantified by many researchers[32-34] in different ways. In the original Brody-Flemings model for a plate dendrite[32],

$$\beta = 2\alpha \quad (4)$$

where  $\alpha$  is a Fourier number.

$$\alpha = \frac{D_S t_f}{X^2} \quad (5)$$

where  $D_S$  is the solute diffusion coefficient in the solid phase,  $t_f$  is the local solidification time, and  $X$  is the length scale of the microsegregation domain, usually taken to equal half of the secondary dendrite arm spacing,  $\lambda_{SDAS}$ ,

$$X = \frac{\lambda_{SDAS}}{2} \quad (6)$$

Eqs. (3) to (6) are solved assuming the known  $t_f$  history to predict  $C_L$  and related microstructure parameters[32]. The Brody-Flemings model simplifies to the Scheil equation in Eq. (2) when  $D_S$  approaches zero ( $\beta = 0$ ). On the other hand, when diffusion in the solid phase is infinitely fast, this model should logically simplify to the other extreme: the Lever rule, Eq. (1), which corresponds to  $\beta = 1$ . Clearly the model with Eq. (4) is not physically reasonable when  $\alpha$  is large and  $\beta$  exceeds 1, because it does not even conserve mass.

To satisfy this requirement, Ohnaka[33] presented a simple modification of  $\beta$  to replace Eq. (4). It is based on comparison with approximate solutions of the diffusion equation for the plate dendrite, assuming a quadratic solute profile in the solid.

$$\beta = \frac{2\alpha}{1 + 2\alpha} \quad (7)$$

A further modification was proposed[33] to account for coarsening and irregular shaped microstructures, such as columnar dendrites, by doubling  $\alpha$  as follows.

$$\beta = \frac{4\alpha}{1 + 4\alpha} \quad (8)$$

Ohnaka has compared concentration predictions using Eqs. (3) and (8) with other approximate solutions, and showed that his model agreed better with experimental data of Matsumiya *et al.*[17] than did predictions with Eq. (4). However, Voller *et al.*[8] pointed out that the performance of this model under constant cooling conditions is significantly better than its performance under parabolic cooling conditions.

A different modification to ensure physical reasonability in the Brody-Flemings model ( $0 < \beta < 1$ ) was proposed by Clyne and Kurz[34] by replacing Eq. (4) as follows.

$$\beta = 2\alpha \left[ 1 - \exp\left(-\frac{1}{\alpha}\right) \right] - \exp\left(-\frac{1}{2\alpha}\right) \quad (9)$$

However, Ohnaka[33] and Matsumiya *et al.*[17] criticized this model for its lack of physical basis for intermediate values of  $\beta$ .

Although all of the above equations for microsegregation are semi-empirical, they are simple analytical models that can be very useful if applied with caution. Among them, the Clyne-Kurz model is the most popular[33]. Kobayashi[35] obtained an exact analytical solution for microsegregation, assuming complete diffusion in the liquid phase, incomplete back-diffusion in the solid phase, constant partition coefficient, constant diffusion coefficient and a parabolic solidification rate. Its predictive performance is better than the above analytical models[35], particularly if the partition coefficient,  $k$ , and Fourier number,  $\alpha$ , are small. But, this analytical solution has the disadvantage that all physical properties must be assumed to be constant, and that the solidification time must be known accurately.

Matsumiya *et al.*[17] solved for interdendritic microsegregation using a 1-D finite-difference numerical method, taking into account the diffusion of solute in both the liquid and the solid phases, and hexagonal morphologies to approximate the dendrites. Battle *et al.*[36] developed a similar numerical model for plate dendrites and included the equation of Kurz *et al.*[44] for isothermal coarsening of the dendrite arms. The approach of Matsumiya *et al.* has been developed further to consider the  $\delta/\gamma$  transformation which occurs during solidification of steels[18]. Wang *et al.*[10] developed a unified solute diffusion model for columnar and equiaxed dendritic alloy solidification, in which nucleation, growth kinetics and dendrite morphology are taken into account. Miettinen[9,37,38] developed models and data for

thermodynamic phase equilibria and diffusion for solidification of low-alloy steels and stainless steels. The predicted thermophysical properties from the melting temperature down to room temperature, including solidus temperatures, solute microsegregation and ferrite contents, agree well with experimental measurements[37]. These models have been implemented into the commercial packages Thermocalc[45], IDS[9] and MAGMA[46]. Unfortunately, these models take longer to compute the solute distribution profile or to couple with other models, so there is still a use for accurate simpler models.

Voller *et al.*[8] proposed that the effect of coarsening can be accounted for in 1-D microsegregation models by adding an additional term to the Fourier number as follows.

$$\alpha^+ = \alpha + \alpha^C \quad (10)$$

This enhancement to the Fourier number accounts for the extra back-diffusion that would occur considering the smaller arm spacing that actually exists during solidification before coarsening. Voller *et al.*[8] showed that, across a wide range of cooling conditions, this model is able to match full coarsening model results by simply adopting a constant value of  $\alpha^C = 0.1$ . They explained that coarsening could be included in any microsegregation model by simply replacing the Fourier number  $\alpha$  with the parameter  $\alpha^+$ .

### III. SIMPLE MICROSEGREGATION MODEL

The present simple microsegregation model developed in this work solves Eqs. (3), (5) and (6) based on evaluating the Clyne-Kurz model for each solute element modified as suggested by Ohnaka[33] to extend the model from plate to columnar dendrites and as suggested by Voller *et al.*[8] to account for coarsening as follows:

$$\beta = 2\alpha^+ \left[ 1 - \exp\left(-\frac{1}{\alpha^+}\right) \right] - \exp\left(-\frac{1}{2\alpha^+}\right), \text{ where } \alpha^+ = 2(\alpha + \alpha^C) \text{ and } \alpha^C = 0.1 \quad (11)$$

This simple semi-empirical analytical model assumes:

- 1) Complete diffusion in the liquid phase.
- 2) Local equilibrium at the solid-liquid interface.
- 3) The equilibrium partition coefficient of solute elements applies at the solid-liquid interface and is constant throughout solidification.
- 4) Nucleation undercooling effects are negligible.
- 5) Fluid flow effects are negligible.

### **A. Secondary Dendrite Arm Spacing Model**

In the present model, the length scale in Eq. (6) is the final secondary dendrite arm spacing,  $\lambda_{SDAS}$ , which varies with cooling conditions and alloy composition. Using  $\lambda_{SDAS}$  measured by several different researchers[47-51] at various cooling rates and steel carbon contents, an empirical relationship was obtained by a best fit as follows,

$$\begin{aligned}\lambda_{\text{SDAS}}(\mu\text{m}) &= (169.1 - 720.9 \cdot C_C) \cdot C_R^{-0.4935} && \text{for } 0 < C_C \leq 0.15 \\ &= 143.9 \cdot C_R^{-0.3616} \cdot C_C^{(0.5501 - 1.996\%C_C)} && \text{for } 0.15 < C_C\end{aligned}\quad (12)$$

where  $C_R$  is the cooling rate ( $^{\circ}\text{C}/\text{sec}$ ) and  $C_C$  is the carbon content (wt%C). Figure 1 compares the predicted and measured  $\lambda_{\text{SDAS}}$  as a function of carbon content at various cooling rates. The  $\lambda_{\text{SDAS}}$  decreases steeply with increasing carbon content from zero to its minimum value at 0.15wt%C, and then increases with increasing carbon content until about 0.6wt%C. From 0.6wt%C to 1.0wt%C,  $\lambda_{\text{SDAS}}$  reduces again with increasing carbon content. This complicated variation of  $\lambda_{\text{SDAS}}$  with carbon content has been noted by other investigators[47,52,53]. El-Bealy *et al.*[52] suggested that this is because different solidification modes control the evolution of structure. Jacobi *et al.*[47] reported that  $\lambda_{\text{SDAS}}$  decreases with increasing carbon content during primary solidification of  $\delta$ -ferrite. When solidification starts with  $\gamma$ -phase, the effect of carbon content is not clear, because only two such alloys (0.59 and 1.48wt%C) were studied. It appears that  $\lambda_{\text{SDAS}}$  decreases with increasing cooling rate for all steels, as shown in Fig. 1. At various cooling rates and carbon contents, the  $\lambda_{\text{SDAS}}$  values predicted with Eq. (12) are in reasonable agreement with the previous experimentally measured data[47-51].

## B. Multicomponent Alloy Effect

In order to extend the model to multicomponent alloys, the effects of all individual components are summed. Mutual interaction effects between the alloying components on microsegregation are neglected. For each component, microsegregation is computed according to Eqs. (3), (5), (6)

and (11), using the individual values for the partition coefficient  $k$  and diffusion coefficient  $D_S$ .

The liquidus temperature,  $T_{liq}$ , depends on steel composition as follows[39],

$$T_{liq} (^{\circ}\text{C}) = T_{pure} - \sum_i m_i \cdot C_{o,i} \quad (13)$$

where  $T_{pure}$  is the melting point of pure iron (1536  $^{\circ}\text{C}$ ) and  $m_i$  is the slope of the liquidus line of each solute element in the pseudo-binary Fe phase diagram, given in Table I[39]. The temperature which corresponds to a given interface composition in the liquid,  $C_{L,i}$ , is found by summing the contributions of all alloying elements (indicated by subscript  $i$ ) :

$$T(^{\circ}\text{C}) = T_{pure} - \sum_i m_i \cdot C_{L,i} \quad (14)$$

where  $k_i$  is the equilibrium partition coefficient of each solute element given in Table I and  $C_{L,i}$  depends on  $f_S$  according to Eqs. (3), (5), (6) and (11). The solidus temperature is given when  $f_S = 1.0$ . The equilibrium solidus temperature can be calculated using the Lever rule, Eqs. (1) and (14).

### C. Peritectic Phase Transformation Effect

In the equilibrium Fe-C phase diagram, two solid phases occur naturally: the  $\delta$ -ferrite phase and the  $\gamma$ -austenite phase. For carbon contents lower than 0.53wt%, when the melt cools down slightly below the liquidus temperature, solid nucleates and grows as  $\delta$ -phase, until solidification

is complete (low carbon content) or until the peritectic temperature is reached (middle carbon content). At the peritectic temperature, solid  $\gamma$ -phase starts to form around the periphery of the  $\delta$ -phase dendrites, where the carbon content is higher. For carbon contents over 0.53wt%, the solid nucleates from the melt as  $\gamma$ -phase, which grows until the end of solidification. These behaviors have important consequences on the metal properties which control microsegregation, as shown in Table I. The equilibrium partition coefficients, diffusion coefficients, and liquidus line slopes of the solute elements depend greatly on the phase, according to measurements[40,41] and extrapolations[39,42,43] from the Fe-X (X = C, Si, Mn, P and S) binary system. The enrichment of solute elements in the interdendritic region during solidification causes a switch from  $\delta$ -phase to  $\gamma$ -phase solidification once the carbon concentration exceeds 0.53wt%C. This change suddenly lowers the diffusion rates, which increases microsegregation and further lowers the solidus temperature.

In order to incorporate the  $\delta/\gamma$  transformation into the present model, the starting temperature,  $T_{start}^{\delta/\gamma}$ , and the ending temperature,  $T_{end}^{\delta/\gamma}$ , of the  $\delta/\gamma$  transformation are needed. The  $\delta/\gamma$  transformation is assumed to start when the solid-liquid interface temperature in Eq. (14) equals the peritectic temperature,  $T_{Ar4}$ , found using the partition coefficients and diffusion coefficient of the  $\delta$ -phase, according to

$$T_{start}^{\delta/\gamma} (^{\circ}\text{C}) = T_{Ar4} = T_{pure}^{\delta/\gamma} - \sum_i n_i \cdot k_i^{\delta/L} \cdot C_{L,i}^{\delta} \quad (15)$$



where  $T_{pure}^{\delta/\gamma}$  is the temperature of the  $\delta/\gamma$  transformation of pure iron (1392 °C),  $n_i$  is the slope of the  $T_{Ar4}$  line of each solute element in its pseudo-binary Fe phase diagram, given in Table I [42],  $k_i^{\delta/L}$  is the equilibrium partition coefficient of each solute element  $i$  of the  $\delta$ -phase and  $C_{L,i}^{\delta}$  is the concentration of each solute element  $i$  in the  $\delta$ -phase at the solid-liquid interface.

The peritectic transformation is assumed to be controlled only by carbon concentration at the solid-liquid interface. The  $\delta/\gamma$  transformation is assumed to be complete when the carbon concentration at the liquid-solid interface becomes equal to 0.53wt%C, based on Eqs. (3), (5), (6) and (11) with the diffusion,  $D_i^{\delta}$ , and partition coefficients,  $k_i^{\gamma/L}$ , of the  $\gamma$ -phase. The corresponding carbon concentration in the solid phase is the triplepoint of the peritectic reaction in the equilibrium Fe-C binary phase diagram[54].

The  $\delta$  fraction of the solid phase is assumed to decrease parabolically from 1 at the start of the  $\delta/\gamma$  transformation to zero at the end, according to

$${}^{\delta}f_S = \left( \frac{f_{end}^{\delta/\gamma} - f_S}{f_{end}^{\delta/\gamma} - f_{start}^{\delta/\gamma}} \right)^2 \cdot f_S \quad (16)$$

When the temperature is above  $T_{Ar4}$  (*i.e.* before the  $\delta/\gamma$  transformation), the solid fraction is entirely  $\delta$ -phase ( $f_S = {}^{\delta}f_S$ ). After the  $\delta/\gamma$  transformation is complete,  ${}^{\delta}f_S$  is zero. The remainder of the solid fraction is naturally  $\gamma$ -phase.

$${}^{\gamma}f_S = f_S - {}^{\delta}f_S \quad (17)$$

Eqs. (16) and (17) are needed to evaluate the average liquid concentrations,  $C_{L,i}^{ave}$ , needed in Eq. (14).

$$C_{L,i}^{ave} = \frac{{}^{\delta}f_S}{f_S} \cdot C_{L,i}^{\delta} + \frac{{}^{\gamma}f_S}{f_S} \cdot C_{L,i}^{\gamma} \quad (18)$$

This equation is needed to evaluate Eq. (14), when both  $\delta$ - and  $\gamma$ -phases are present.

#### D. Cooling History Effect

The local solidification time,  $t_f$ , needed in Eq. (5) is found from the cooling history. For the constant cooling rate assumed in the present work, this simplifies to:

$$t_f = \frac{T_{liq} - T_{sol}}{C_R} \quad (19)$$

A first estimate of the local solidification time is chosen by evaluating the equilibrium liquidus and solidus temperatures from Eq. (13), and the Lever rule, Eqs. (1) and (14), respectively. From this initial guess, the value of  $T_{sol}$  is improved with a few iterative steps through Eqs. (12), (6), (19), (5), (11), (3), and (14) until consistent values are found for  $C_{L,i}$ ,  $f_S$  and  $T$  (e.g.  $f_S = 1$  at  $T_{sol}$ ). If Eq. (15) indicates that two-phase conditions are present, then Eqs. (16)-(18) are used to

transform separate sets of  $C_{L,i}$  values for the  $\gamma$  and  $\delta$ -phases from the results of Eq. (13) to find the single set of  $C_{L,i}^{ave}$  values needed in Eq. (14). In practice, it is often desirable to find the entire solid fraction and temperature relationship. Thus, it is convenient to solve these equations simply by trial and error by systematically incrementing the solid fraction from 0 to 1 in steps of 0.001.

#### IV. FINITE DIFFERENCE MODEL

In order to help validate the present simple model, the one-dimensional direct finite difference model based on that of Ueshima *et al.*[18] was developed and implemented to track the liquid fraction,  $\delta$ -phase solid fraction,  $\delta f_s$ , and  $\gamma$ -phase solid fraction,  $\gamma f_s$ , in the mushy zone as a function of temperature and to calculate solute redistribution. This model solves the following diffusion equations in a hexagonal domain chosen to approximate the morphology of columnar dendrites as shown in Figure 2.

$$\frac{\partial C_{S,i}}{\partial t} = \frac{\partial}{\partial x} \left( D_{S,i}(T) \frac{\partial C_{S,i}}{\partial x} \right) \quad (20)$$

Complete mixing of solute elements in the liquid phase and local equilibrium at the liquid/ $\delta$ , liquid/ $\gamma$  and  $\delta$ / $\gamma$  interfaces are assumed. Diffusion of solute along the axial direction of the dendrite is assumed to be negligible. Thus, the model ignores macrosegregation due to fluid flow. As for the simple model, the equilibrium partition coefficients, diffusion coefficients and the slope of the liquidus line of the solute elements are given in Table I. The secondary dendrite

arm spacing used in this study is given in Eq. (12) as functions of cooling rate and carbon content. The calculation was made by dividing the triangular transverse cross section into 100 thin nodal areas as shown in Figure 3. Initial and boundary conditions are:

$$\begin{aligned}
 \text{I. C. } & C_{S,i} = k^{S/L} \cdot C_{o,i} \quad \text{at } t = 0 \\
 \text{B.C. } & \frac{\partial C_{S,i}}{\partial x} = 0 \quad \text{at } x = 0, \lambda_{SDAS}/2
 \end{aligned} \tag{21}$$

When the liquidus temperature,  $T_{liq}$ , and the  $\delta/\gamma$  transformation temperature,  $T_{Ar4}$ , become equal to the actual temperature of a given nodal area, the solidification and  $\delta/\gamma$  transformation in that area are assumed to be complete and the interfaces move to the adjacent area.  $T_{liq}$  and  $T_{Ar4}$  are calculated using Eqs. (13) and (15), respectively. Further information on this model is presented elsewhere[17-20].

## V. MODEL VALIDATION

To assess the validity of the present models, the microsegregation predictions were compared with previous microsegregation results in three different systems where measurements and/or numerical solutions were available.

### A. Eutectic Formation in Aluminum Alloys

The first test is for an aluminum alloy with 4.9%Cu where final eutectic volume fraction was measured[21,55]. A eutectic fraction prediction is readily obtained from Eqs. (3), (5), (6) and

(11) of the simple model on setting  $C_L = 33.2\%Cu$  for this binary system. Figure 4 compares the predicted eutectic volume fraction of the simple model as a function of cooling rate (or solidification time) with experimental measurements of Sarreal *et al.*[21] and the numerical prediction by Voller *et al.*[8] for the conditions of  $k = 0.145$ [36],  $D_S$  (cm<sup>2</sup>/sec) =  $5 \times 10^{-9}$ [8],  $\lambda_{SDAS}$  ( $\mu\text{m}$ ) =  $46.6 \cdot C_R^{-0.29}$ [21] and  $T_{liq}$  ( $^{\circ}\text{C}$ ) =  $660 - 3.374 \cdot (\%Cu)$  for this binary system. The measured eutectic volume fractions[21] are given in Table II, based on conversions from the measured non-equilibrium second phase[55]. The predicted eutectic fractions from the simple model are in reasonable agreement with these measurements.

## B. Segregation in Liquid Steel

The second validation of the simple model investigated microsegregation of manganese and carbon for steel M1 in Table III. For this test, the manganese concentration predicted by the simple model was compared with results of the complete finite-difference model (Section IV) and other simple models including the Lever rule in Eq. (1), Scheil Eq. (2), and the different forms of Eq. (3) including the equations of Brody-Flemings Eq. (4), Ohnaka Eqs. (7) and (8), and Clyne-Kurz Eq. (9). The results are compared in Figure 5 for assumed conditions of  $X = 180$   $\mu\text{m}$ ,  $D_S = 1.378 \times 10^{-7}$  cm<sup>2</sup>/sec,  $t_f = 879.2$  sec,  $k = 0.77$  and  $C_o = 1.52$  based on the property data in Table I. The simple model is in good agreement with the present finite difference model. The Brody-Fleming equation and Ohnaka Eq. (8) also predict nearly the same microsegregation. However, the original of Clyne-Kurz equation and Ohnaka Eq. (7) predict slightly higher microsegregation, with almost identical values, as shown in Table IV.

Figure 6 compares the changes of the carbon concentration in the liquid phase at the solid-liquid interface. For the conditions of  $X = 180 \mu\text{m}$ ,  $D_S = 7.263 \times 10^{-6} \text{cm}^2/\text{sec}$ ,  $t_f = 168.3 \text{ sec}$ ,  $k = 0.19$  and  $C_o = 0.13$ , all equations except the Scheil and Brody-Fleming equations, predict almost the same microsegregation. As Clyne and Kurz[34] explained, when  $\alpha$  is large, the Brody-Flemings equation predicts less enrichment in the liquid phase than does the Lever rule, so is physically unreasonable. The Scheil equation naturally over predicts the enrichment. The other models predict similar large  $\beta$  values, so their liquid concentration predictions are similar, as shown in Table IV. Even the Lever rule ( $\beta = 1$ ) is quite reasonable, as carbon diffusion is almost complete for the large value of  $\alpha$  in this problem (3.773). In summary, the liquid concentrations of the present simple model agree well for a wide range of  $\alpha$ , as shown in Figs. 4, 5 and 6.

For the next validation test, model predictions are compared with the experimental measurements by Matsumiya *et al.*[17] for steel M1, which was solidified unidirectionally and quenched with a columnar structure at two different cooling rates. The measured primary dendrite arm spacing was  $360 \mu\text{m}$  at cooling rates of  $0.045$  and  $0.25 \text{ }^\circ\text{C}/\text{sec}$ . The secondary dendrite arm spacing was  $100 \mu\text{m}$  at  $0.25 \text{ }^\circ\text{C}/\text{sec}$ . But, at  $0.045 \text{ }^\circ\text{C}/\text{sec}$ , the dendrites in the microstructure did not exhibit clear patterns for secondary dendrite arm spacing. Although it is not exactly clear, the measurement appears to be some average of the solute concentration in the quenched region, including both interdendritic primary arm and interdendritic secondary arm material. Accordingly, calculations were performed with both microsegregation models for the primary arm spacing of  $360 \mu\text{m}$  at  $0.045 \text{ }^\circ\text{C}/\text{sec}$ , and for the secondary arm spacing of  $100 \mu\text{m}$  at  $0.25 \text{ }^\circ\text{C}/\text{sec}$ . Calculations were also performed using the secondary dendrite arm spacing obtained from Eq. (12).

Figure 7 compares the calculated manganese and phosphorus concentrations in the liquid phase at the solid-liquid interface. All calculations fall between the experimental measurements for both cooling rates, as shown in Fig. 7. The results using spacings from Eq. (12), are almost identical for both cooling rates as for 0.045 °C/sec with the primary dendrite arm spacing of 360 μm. This is because the parameter  $t_f / X^2$  is about the same, as shown in Table V. The relative accuracy of all of these similar predictions could not be resolved within the experimental uncertainty.

### **C. Solidification Temperatures of Steel**

The final three validation tests focus on the non-equilibrium 75%-solid and solidus temperatures for three different steel systems at three different cooling rates. These two solid fractions are chosen because they are believed[20] to correlate with the sudden mechanical property changes observed during high temperature tensile tests with *in-situ* melting[22-26]. Specifically, these measurements have identified a zero strength temperature (ZST) and a zero ductility temperature (ZDT). Above ZST, solidifying steel has no strength and no ductility, and behaves as a liquid. At temperatures between ZST and ZDT, the steel has no ductility, but does have some strength due to the mechanical network between dendrites. As long as some liquid remains, the steel fails in a brittle manner due to rapid strain concentration and failure of the interdendritic liquid film. Below ZDT, the solidifying steel behaves as a solid with both strength and ductility.

The ZDT should, theoretically, be found at the non-equilibrium solidus temperature, where the solid fraction  $f_s$  approaches 1. Won *et al.*[20] reported that the critical solid fraction at zero strength temperature corresponds to 0.75, based on a statistical assessment of microsegregation measurements and a finite difference model at various carbon contents and cooling rates.

Non-equilibrium pseudo Fe-C phase diagrams are calculated using both the simple model and the present finite difference model, and are compared with ZST and ZDT measurements[22-24] in Figures 8, 9 and 10. The experiments were performed by melting steel samples in a quartz tube and conducting tensile tests on the solidifying steel using a Gleeble system. For the calculations, the length scale was calculated using  $\lambda_{SDAS}$  from Eq. (12) and the steel compositions are given in Table III.

The non-equilibrium phase diagram in Figure 8 is calculated for steel S1 and compared with the ZST and ZDT measurements of Shin *et al.*[22] at a cooling rate of 0.17 °C/sec and a strain rate of 0.01 sec<sup>-1</sup>. The calculated ZDT is only 1.24 ~ 4.24 °C below the equilibrium solidus temperature, as shown in Table VI. Figure 9 is based on steel S2 for the ZST and ZDT measurements of Seol *et al.*[23] at 1.0 °C/sec and 0.01 sec<sup>-1</sup>. The calculated undercooling of ZDT below the equilibrium solidus temperature increases from 2.65 to 17.25 °C with increasing carbon content. Figure 10 is based on steel S3 and compared with the measurements of Schmidtman *et al.*[24] at 10 °C/sec and 0.2 sec<sup>-1</sup>. The calculated undercooling of ZDT increases from 3.73 to 31.09 °C with increasing carbon content, as shown in Table VI.



The extent of segregation-related undercooling of the final solidification temperature (ZDT) increases both with increasing carbon content and with increasing the alloy content from steel S1 (Fig. 8) to S2 (Fig. 9) to S3 (Fig. 10). Increasing carbon content extends the mushy zone. More importantly, the liquid concentration can exceed 0.53%C more easily, so  $\gamma$ -phase is more likely to form during solidification. For carbon contents less than about 0.1wt%, the  $\delta/\gamma$  transformation takes place after solidification, so segregation undercooling is small. With greater carbon contents, some  $\gamma$ -phase forms during solidification. Diffusion through the closer-packed austenite structure is slower, so microsegregation increases and depresses the solidus temperature further below equilibrium. In particular, the segregation of S and P becomes increasingly important with increasing freezing range and austenite fraction. This is because these elements also have very low partition coefficients, which are even smaller for  $\gamma$ -phase than for  $\delta$ -phase. Finally, the increasing depression of the solidus temperature from steels S1 to S2 to S3 is also caused in part by the increasing cooling rate for these three case studies.

In all three figures 8 to 10, the measured ZST and ZDT data roughly agree with the calculated temperatures at which the solid fraction becomes 0.75 and 1.0, respectively. The results of the simple model also agree with those of the finite difference model. The slight discrepancy for 0.1 ~ 0.2wt%C steels is because the simple model does not account for the diffusion between solid phases that affects the peritectic reaction. Even so, the calculated starting temperature,  $T_{start}^{\delta/\gamma}$ , and ending temperature,  $T_{end}^{\delta/\gamma}$ , of the  $\delta/\gamma$  transformation roughly agree between the two models.

Figure 11 compares predictions of the simple microsegregation model with experimentally measured liquidus[27-30], solidus[27-30], peritectic temperatures[27-29], ZST[22-24,26] and

ZDT[22-26]. The liquidus, solidus and peritectic temperatures were obtained by differential thermal analysis (DTA) at a range of slow cooling rates [27-30]. All calculations are in reasonable agreement with the measurements, although there is more scatter in the solidus temperature predictions. The ZST and ZDT measurements[22-26] agree well, as discussed previously. In summary, these test results show that the proposed simple microsegregation model can reasonably simulate a range of solidification phenomena, especially for steel.

#### **D. Discussion**

The solidus temperature measured by DTA is generally greater than the measured ZDT for the same conditions, especially for high carbon content. This is because the DTA measurement has difficulty detecting the solidification of the last few percent of liquid[56] which is found segregated at the grain boundaries and governs ZDT. The present model assumes these two temperatures are the same, and better predicts the ZDT, so solidus temperatures are naturally underestimated in high carbon steels, as shown in Fig. 11. The model thus appears to empirically incorporate both interdendritic and grain boundary segregation. A more sophisticated model might simulate both interdendritic microsegregation and macrosegregation at the grain size scale to account for the differences between grain boundary and interdendritic liquid. Such a model could resolve the apparent discrepancy by matching both measurements. Further research is needed with both modeling and measurements in order to quantify the behavior of alloys in steel during the final stages of solidification.

## **VI. EFFECTS OF COOLING RATE AND SECONDARY DENDRITE ARM SPACING**

The present simple microsegregation model was next applied to investigate the effects of cooling rate and secondary dendrite arm spacing on microsegregation for three steel compositions of 0.044, 0.18 and 0.8wt%C with 0.34%Si-1.52%Mn-0.012%P-0.015%S (*i.e.* based on steel S3 in Table III). To isolate the effect of cooling rate alone on microsegregation, the secondary dendrite arm spacings are first assumed to be constants of 44.1, 45.1 and 79.0  $\mu\text{m}$  for carbon contents of 0.044, 0.18 and 0.8wt%C, respectively. Figure 12 shows the phase fraction results calculated with the present model as a function of temperature. The calculated non-equilibrium solidus temperature for all three steels decreases with increasing cooling rate from 1 to 100  $^{\circ}\text{C}/\text{sec}$ . The extent of the decrease increases from 3 to 74  $^{\circ}\text{C}$  for alloy content increasing from 0.044 to 0.8wt%C.

To isolate the effect of length scale alone on microsegregation, the cooling rate is fixed at 10  $^{\circ}\text{C}/\text{sec}$  for three different secondary dendrite arm spacings. Figure 13 shows the evolution of the phase fractions for the various spacings and steel compositions. The calculated non-equilibrium solidus temperature decreases slightly with increasing secondary dendrite arm spacing. The extent of the decrease increases from 12 to 50  $^{\circ}\text{C}$  for alloy content increasing from 0.044 to 0.8wt%C.

The solidus temperature has just been shown to decrease with both increasing cooling rate and increasing secondary dendrite arm spacing. In real casting processes, the secondary dendrite arm spacing itself evolves during solidification, specifically decreasing with increasing cooling rate. In the surface region, the secondary dendrite arm spacing is small, because the cooling rate is

high due to the large heat extraction. In the interior, the secondary arm spacing is larger due to the slower cooling rate. Thus, the two opposite effects should partially cancel in a real casting.

In order to investigate the combined effects of cooling rate and secondary dendrite arm spacing, calculations were performed with both microsegregation models at the three cooling rates of 1, 10 and 100 °C/sec using the secondary dendrite arm spacing obtained from Eq. (12). Figure 14 shows the evolution of the phase fractions as a function of temperature for the conditions given in Table VII. As expected, the phase fractions calculated at 1 °C/sec are nearly the same as those at 100 °C/sec, because the secondary dendrite arm spacing decrease with increasing cooling rate. This shows that decrease in solidus temperature caused by increasing cooling rate is almost cancelled by the increase in solidus temperature accompanying the closer secondary dendrite arm spacing. For the 0.044wt%C steel, the solidus temperatures are the same within  $\pm 0.1$  °C, as shown in Table VIII part 3. For 0.18 and 0.8wt%C steels, the solidus temperatures still decrease by 7.6 and 17.9 °C, respectively, due to the combined effects of increasing cooling rate from 1 to 100 °C/sec. The effect of cooling rate is more important than that of secondary dendrite arm spacing, so the cancellation is not perfect. However, these small differences contrast with the 20 ~ 70 °C changes in solidus temperatures predicted with independent changes in cooling rate or secondary dendrite arm (See Table VIII parts 1 and 2).

## **VII. NON-EQUILIBRIUM PHASE DIAGRAM AND CRACK FORMATION**

Figure 15 shows the non-equilibrium pseudo Fe-C phase diagram for steel S3 at cooling rates of 1, 10 and 100 °C/sec using the present analytical model. The secondary dendrite arm spacings

from Eq. (12) vary with both carbon content and cooling rate. For this model, the solid fractions of 0.0, 0.75, 0.9 and 1.0 are believed to correspond to the characteristic temperatures of  $T_{liq}$ , zero strength temperature (ZST), liquid impenetrable temperature (LIT) and zero ductility temperature (ZDT), respectively.

The ability to accurately predict these temperatures is of practical consequence to the prediction, understanding and avoidance of cracks, such as hot tears. Cracks which form above the LIT, are refilled with liquid fed in from the bulk. Cracks, which form below LIT cannot refill, however, because the dendrite arms are close enough to resist feeding of the liquid. This critical temperature is proposed to correspond to a solid fraction of 0.9[19,57,58]. Figure 15 shows that the combined effects of cooling rate and secondary dendrite arm spacing on  $T_{liq}$ , ZST and LIT is not significant. However, the combined effects on ZDT are significant in steels above 0.1wt%C with high alloy content. This is due to the enhanced segregation of solute elements near the final stage of solidification and the lower partition coefficients for the  $\gamma$ -phase, relative to  $\delta$ . With increasing carbon content, increasing the cooling rate lowers ZDT more, which increases the critical temperature range between LIT and ZDT. This suggests that the tendency for cracking during solidification should increase with increasing cooling rate, with increasing carbon content above 0.1wt%C and with increasing alloy content.

Further complexities arise due to flow and macrosegregation, non-uniform heat transfer, thermal-mechanical deformation, and stress concentration. Further work is needed to incorporate the simple model presented here into other advanced macroscopic models to simulate fluid flow, heat transfer and stress during solidification processes.

## VIII. CONCLUSIONS

A simple analytical model of microsegregation based on the Clyne-Kurz model has been developed, which takes into account the effects of multiple components, columnar dendrites, coarsening and the  $\delta/\gamma$  transformation for application to the solidification of steels. A new empirical equation for the secondary dendrite arm spacing, which varies with cooling rate and carbon content, has been proposed, based on measurements by several different researchers as follows.

$$\begin{aligned}\lambda_{\text{SDAS}} (\mu\text{m}) &= (169.1 - 720.9 \cdot C_C) \cdot C_R^{-0.4935} && \text{for } 0 < C_C \leq 0.15 \\ &= 143.9 \cdot C_R^{-0.3616} \cdot C_C^{(0.5501 - 1.996 \cdot \%C_C)} && \text{for } 0.15 < C_C\end{aligned}$$

Predictions with this microsegregation model agree with both experimental measurements and calculations with a detailed finite difference model. Model predictions for a range of steel compositions, cooling rates and secondary dendrite arm spacings reveal:

- 1) The solidus temperature is lowered significantly with independent increases in either cooling rate or secondary dendrite arm spacing.
- 2) In real castings, where spacings change with cooling rate, the effect of cooling rates less than 100 °C/sec on phase fraction evolution is insignificant in low alloy steels with less than 0.1wt%C, and for phase fractions below 0.9 in other steels.

3) Solute element concentration, especially phosphorus and sulfur, has a significant effect on solidus temperature and zero ductility temperature due to their enhanced segregation near the final stage of solidification.

The simple analytical model presented here can easily and efficiently incorporate microsegregation phenomena into solidification calculations for use in advanced macroscopic models.

## NOMENCLATURE

$C_C$	average carbon concentration (wt%)
$C_{L,i}^{ave}$	average liquid concentration during the $\delta/\gamma$ transformation (wt%)
$C_L$	liquid concentration (wt%)
$C_o$	initial liquid concentration (wt%)
$C_R$	cooling rate ( $^{\circ}\text{C}/\text{sec}$ )
$D_S$	diffusion coefficient ( $\text{cm}^2/\text{sec}$ )
$f_S$	solid fraction
$f_{end}^{\delta/\gamma}$	ending solid fraction of $\delta/\gamma$ transformation
$f_{start}^{\delta/\gamma}$	starting solid fraction of $\delta/\gamma$ transformation
${}^{\delta}f_S$	$\delta$ -phase fraction in the solid phase
${}^{\gamma}f_S$	$\gamma$ -phase fraction in the solid phase
$i$	solute element (carbon, silicon, manganese, phosphorus or sulfur)
$k$	equilibrium partition coefficient
$m$	slope of the liquidus line ( $^{\circ}\text{C}/\%$ )
$n$	slope of the $T_{Ar4}$ line ( $^{\circ}\text{C}/\%$ )
$T_{liq}$	liquidus temperature ( $^{\circ}\text{C}$ )
$T_{pure}$	melting point of pure iron (1536 $^{\circ}\text{C}$ )
$T_{sol}$	solidus temperature ( $^{\circ}\text{C}$ )
$T_{Ar4}$	$Ar_4$ transformation temperature ( $^{\circ}\text{C}$ )
$T_{end}^{\delta/\gamma}$	ending temperature of $\delta/\gamma$ transformation ( $^{\circ}\text{C}$ )



$T_{pure}^{\delta/\gamma}$	temperature of $\delta/\gamma$ transformation of pure iron (1392 °C)
$T_{start}^{\delta/\gamma}$	starting temperature of $\delta/\gamma$ transformation (°C)
$t$	time (sec)
$t_f$	local solidification time (sec)
$X$	length scale of the microsegregation domain
$x$	width of the nodal area
$\alpha$	Fourier number, Eq. (5)
$\alpha^+$	Fourier number accounts for coarsening
$\alpha^C$	extra back-diffusion from coarsening = 0.1
$\beta$	back-diffusion parameter
$\lambda_{SDAS}$	secondary dendrite arm spacing ( $\mu\text{m}$ )

## REFERENCES

1. M. C. Flemings and G. E. Nereo : Macrosegregation; Part1, *Trans. Met. Soc. AIME*, 1967, vol. 239, pp. 1449-61.
2. R. Mehrabian, M. Keane and M. C. Flemings : Interdendritic fluid flow and macrosegregation; Influence of gravity, *Metall. Trans.*, 1970, vol. 1, pp. 1209-20.
3. T. Fuji, D. R. Poirier and M. C. Flemings : Macrosegregation in a multicomponent low alloy steel, *Metall. Trans. B*, 1979, vol. 12B, pp. 331-39.
4. H. Mizukami, M. Komatsu, T. Kitagawa and K. Kawakami : *Trans. Iron Steel Ins. Japan*, 1984, vol. 24, pp. 940-49.
5. K. S. Oh, I. R. Lee, Y. K. Shin, Y. S. Koo, I. J. Lee and D. Y. Lee : Proc. 6th Int. Iron Steel Cong., Nagoya, ISIJ, 1990, pp. 256-63.
6. K. Ayata, S. Koyama, H. Nakata, S. Kawasaki, K. Ebina and T. Hata : Proc. 6th Int. Iron Steel Cong., Nagoya, ISIJ, 1990, pp. 279-84.
7. M. El-Bealy : On the mechanism of halfway cracks and macro-segregation in continuously cast steel slabs, *Scand. J. Metall.*, 1995, vol. 24, pp. 63-80.
8. V. R. Voller and C. Beckermann : A unified model of microsegregation and coarsening, *Metall. Trans. A*, 1999, vol. 30A, pp. 2183-89.
9. J. Miettinen : Mathematical simulation of interdendritic solidification of low-alloyed and stainless steels, *Metall. Trans. A*, 1992, vol. 23A, pp. 1155-70.
10. C. Y. Wang and C. Beckermann : A unified solute diffusion-model for columnar and equiaxed dendritic alloy solidification, *Mater. Sci. Eng.*, 1993, vol. 171, pp. 199-211.
11. J. F. M<sup>C</sup>Carthy : Phase diagram effects in phase field models of dendritic growth in binary alloys, *Acta Mater.*, 1997, vol. 45, pp. 4077-91.

12. A. Karma and W. J. Rappel : Quantitative phase-field modeling of dendritic growth in two and three dimensions, *Physical Review D*, vol. 57, pp. 4323-49.
13. J. Tiaden : Phase field simulations of the peritectic solidification of Fe-C, *J. of Crystal Growth*, 1999, vol. 199, pp. 1275-80.
14. J. S. Lee, S. G. Kim, W. T. Kim and T. Suzuki : Numerical simulation of peritectic reaction using a multi-phase-field model, *ISIJ International*, 1999, vol. 39, pp. 730-36.
15. B. Nestler and A. A. Wheeler : A multi-phase-field model of eutectic and peritectic alloys: Numerical simulation of growth structures, *Physica D*, 2000, vol. 138, pp. 114-33.
16. J. Rappaz and J. F. Scheid : Existence of solutions to a phase-field model for the isothermal solidification process of a binary alloy, *Math. Methods Appl. Sci.*, 2000, vol. 23, pp. 491-513.
17. T. Matsumiya, H. Kajioka, S. Mizoguchi, Y. Ueshima and H. Esaka : Mathematical analysis of segregations in continuously-cast slabs, *Trans. ISIJ*, 1984, vol. 24, pp. 873-82.
18. Y. Ueshima, S. Mizoguchi, T. Matsumiya and H. Kajioka : Analysis of solute distribution in dendrites of carbon steel with  $\delta/\gamma$  transformation during solidification, *Metall. Trans. B*, 1986, vol. 17B, pp. 845-59.
19. K. Kim, T. Yeo, K. H. Oh and D. N. Lee : Effect of carbon and sulfur in continuously cast strand on longitudinal surface crack, *ISIJ International*, 1996, vol. 36, pp. 284-89.
20. Y. M. Won, K. H. Kim, T. Yeo and K. H. Oh : Effect of cooling rate on ZST, LIT and ZDT of carbon steels near melting point, *ISIJ International*, vol. 38, 1998, pp. 1093-99.
21. J. A. Sarreal and G. J. Abbaschian : The effect of solidification rate on microsegregation, *Metall. Trans. A*, 1986, vol. 17A, pp. 2063-73.
22. G. Shin, T. Kajitani, T. Suzuki and T. Umeda : Mechanical properties of carbon steels during solidification, *Tetsu-to- Hagané*, 1992, vol. 78, pp. 587-93.

23. D. J. Seol, Y. M. Won, K. H. Oh, Y. C. Shin and C. H. Yim : Mechanical behavior of carbon steels in the temperature range of mushy zone, *ISIJ International*, vol. 40, 2000, pp. 356-63.
24. E. Schmidtman and F. Rakoski : Influence of the carbon content of 0.015 to 1% and of the structure on the high-temperature strength and toughness behavior of structural steels after solidification from the melt, *Arch. Eisenhüttenwes.*, 1983, vol. 54, pp. 357-62.
25. H. G. Suzuki, S. Nishimura and Y. Nakamura : Improvement of hot ductility of continuously cast carbon steels, *Trans. ISIJ*, 1984, vol. 24, pp. 54-59.
26. T. Nakagawa, T. Umeda, J. Murata, Y. Kamimura and N. Niwa : Deformation behavior during solidification of steels, *ISIJ International*, 1995, vol. 35, pp. 723-29.
27. *A Guide to the Solidification of Steels*, Jernkontoret, Stockholm, 1977.
28. L. Ericson : Cracking in low alloy aluminum grain refined steels, *Scand. J. Metall.*, 1977, vol. 6, pp. 116-24.
29. S. Kobayashi : A mathematical model for solute redistribution during dendritic solidification, *Trans. Iron Steel Inst. Jpn.*, 1988, vol. 28, pp. 535-42.
30. Y. C. Shin, J. Choi and C. H. Yim : Technical Report, Iron & Steel Making Research Team, Technical Research Labs., POSCO, Korea, 1998.
31. E. Scheil : Bemerkungen zur Schichtkristallbildung, *Z. Metallkd.*, 1942, vol. 34, pp. 70-72.
32. H. D. Brody and M. C. Flemings : Solute redistribution in dendritic solidification, *Trans. Metall. Soc. AIME*, 1966, vol. 236, pp. 615-24.
33. I. Ohnaka : Mathematical analysis of solute redistribution during solidification with diffusion in solid phase, *Trans. ISIJ*, 1986, vol. 26, pp. 1045-51.
34. T. W. Clyne and W. Kurz : Solute redistribution during solidification with rapid solid state diffusion, *Metall. Trans. A*, 1981, vol. 12A, pp. 965-71.

35. S. Kobayashi : Solute redistribution during solidification with diffusion in solid phase; A theoretical analysis, *J. Crystal Growth*, 1988, vol. 88, pp.87-96.
36. T. P. Battle and R. D. Pehlke : Mathematical modeling of microsegregation in binary metallic alloys, *Metall. Trans. B*, 1990, vol. 21B, pp. 357-75.
37. J. Miettinen : Simple semiempirical model for prediction of austenite decomposition and related heat release during cooling of low alloyed steels, *Ironmaking and Steelmaking*, 1996, vol. 23, pp. 346-56.
38. J. Miettinen : Calculation of solidification-related thermophysical properties for steels, *Metall. Trans. B*, 1997, vol. 28B, pp. 281-97.
39. T. Kawawa : Tekko-no-Gyoko (Solidification of Steel), ed. by Solidification Comm. of ISIJ, ISIJ, Tokyo, 1977, Appendix, 13.
40. Y. Nakamura and H. Esaka : *Tetsu-to- Hagané*, 1981, vol. 67, p. S140.
41. Tekko-no-Gyoko (Solidification of Steel), supplement, Solidification Comm. of ISIJ, ISIJ, Tokyo, 1977, pp. S32-S50.
42. Metal Handbook, ed. By T. Lyman, H. E. Boyer, W. J. Carnes and M. W. Chevalier, 8th ed., ASM, Metal Park, OH, 1973.
43. Tekko-Binran (Handbook for Steel), by ISIJ, rd ed., Maruzen, Tokyo, 1981, vol. 1, pp. 193-94.
44. W. Kurz and D. J. Fisher: Fundamentals of Solidification, Trans. Tech., Aedermansdorf, 1989.
45. B. Sundman, B. Jansson and J. –O. Andersson : *CALPHAD*, 1985, vol. 9, pp. 153-90.
46. E. Flender : MAGMASOFT, Magma Gmbh, Aachen, Germany, 2000.
47. H. Jacobi and K. Wünnenberg : Solidification structure and micro-segregation of unidirectionally solidified steels, *Steel Research*, 1999, vol. 70, pp. 362-67.

48. B. Weisgerber, M. Hecht and K. Harste : Investigations of the solidification structure of continuously cast slabs, *Steel Research*, 1999, vol. 70, pp. 403-11.
49. M. Imagumbai and T. Takeda : Influence of calcium-treatment of sulfide- and oxide-inclusions in continuous-cast slab of clean steel – dendrite structure and inclusions, *ISIJ International*, 1994, vol. 34, pp. 574-83.
50. D. Senk, B. Engl, O. Siemon and G. Stebner : Investigation of solidification and microsegregation of near-net-shape cast carbon steel, *Steel Research*, 1999, vol. 70, pp. 368-72.
51. A. Suzuki, T. Suzuki, Y. Nagaoka and Y. Iwata : On secondary dendrite arm spacing in commercial carbon steels with different carbon content, *Nippon Kinzoku Gakkaishi*, 1968, vol. 32, pp. 1301-05.
52. M. El-Bealy and B. G. Thomas : Prediction of dendrite arm spacing for low alloy steel casting processes, *Metall. Trans. B*, 1996, vol. 27B, pp. 689-93.
53. D. J. Hurtuk and A. A. Tzavaras : Aberrations observed in the relationship of dendrite size-alloying elements for low-alloy steel, Proc. Inter. Conf. on Solidification, Solidification and Casting of Metals, Univ. of Sheffield, 1977, pp. 21-28.
54. T. B. Massalski : Binary Alloy Phase Diagrams, vol. 1, ASM, Materials Park, 1986, p. 842.
55. V. R. Voller and S. Sundarraj : Modeling of microsegregation, *Mater. Sci. Technol.*, 1993, vol. 9, pp. 478-81.
56. A. A. Howe : Estimation of liquidus temperatures for steels, *Ironmaking and Steelmaking*, 1988, vol. 15, pp. 134-42.
57. T. W. Clyne, M. Wolf and W. Kurz : The effect of melt composition on solidification cracking of steel, with particular reference to continuous casting, *Metall. Trans. B*, 1982, vol. 13B, pp. 259-66.

58. Y. M. Won, T. Yeo, D. J. Seol and K. H. Oh : A new criterion for internal crack formation in continuously cast steels, *Metall. Trans. B*, 2000, vol. 31B, pp. 779-94.

## TABLE LIST

Table I. Equilibrium partition coefficients, diffusion coefficients and liquidus line slopes of the solute elements[39-43].

Table II. Data for Al-4.9%Cu alloy experiments[21].

Table III. Chemical compositions of carbon steels (wt%) and cooling rates ( $^{\circ}\text{C}/\text{sec}$ ).

Table IV. Different microsegregation equation predictions of  $\beta$  for two sets of conditions ( $\alpha$  values).

Table V. Variation of parameter  $t_f/X^2$  at conditions for steel M1 (Table III).

Table VI. Calculated solidus temperature using the Lever rule and simple model for steels S1, S2 and S3 (Table III).

Table VII. Calculated secondary dendrite arm spacings from Eq. (12) for steel S3 (Table III).

Table VIII. Calculated solidus temperatures using the simple model for steel S3 (Table III).



Table I. Equilibrium partition coefficients, diffusion coefficients and liquidus line slopes of the solute elements[39-43].

Element	$k^{\delta/L}$	$k^{\gamma/L}$	$D^{\delta}$ (cm <sup>2</sup> /sec)	$D^{\gamma}$ (cm <sup>2</sup> /sec)	$m$ (°C/%)	$n$ (°C/%)
C	0.19	0.34	0.0127exp(-19450/RT)	0.0761exp(-32160/RT)	78.0	-1122
Si	0.77	0.52	8.0exp(-59500/RT)	0.3exp(-60100/RT)	7.6	60
Mn	0.76	0.78	0.76exp(-53640/RT)	0.055exp(-59600/RT)	4.9	-12
P	0.23	0.13	2.9exp(-55000/RT)	0.01exp(-43700/RT)	34.4	140
S	0.05	0.035	4.56exp(-51300/RT)	2.4exp(-53400/RT)	38.0	160

Notes : R is gas constant in cal/mol and T is temperature in K.

Table II. Data for Al-4.9%Cu alloy experiments[21].

$C_R$ (°C/sec)	$t_f$ (sec)	$\lambda_{SDAS}$ (μm)	Eutectic fraction (%)
0.1	980	91	5.54
1.05	93.3	46	6.52
11.25	8.72	23	6.84
65	1.51	14	7.16
187	0.52	10	7.50

Table III. Chemical compositions of carbon steels (wt%) and cooling rates (°C/sec).

Sample	C	Si	Mn	P	S	$C_R$	Ref.
M1	0.13	0.35	1.52	0.016	0.002	0.045, 0.25	[17]
S1	0.06-0.6	0.015	1.05	0.0009	0.0008	0.17	[22]
S2	0.12-0.81	0.24	0.61	0.015	0.009	1	[23]
S3	0.015-1.0	0.34	1.52	0.012	0.015	10	[24]

Table IV. Different microsegregation equation predictions of  $\beta$  for two sets of conditions ( $\alpha$  values).

$\alpha$	$\beta$						
	Eq. (1)	Eq. (2)	Eq. (4)	Eq. (7)	Eq. (8)	Eq. (9)	Eq. (11)
0.3738	1	0	0.7476	0.4278	0.5992	0.4336	0.6455
3.773	1	0	7.546	0.8830	0.9376	0.8810	0.9388

Table V. Variation of parameter  $t_f/X^2$  at conditions for steel M1 (Table III).

	Assumed DAS		$\lambda_{SDAS}$ in Eq. (12)	
	0.045	0.25	0.045	0.25
$C_R$ ( $^{\circ}\text{C}/\text{sec}$ )	0.045	0.25	0.045	0.25
$X$ ( $\mu\text{m}$ )	180	50	174	74.5
$t_f$ (sec)	879.2	143.9	835.5	150.6
$t_f/X^2$ ( $\times 10^{-2}$ sec/ $\mu\text{m}^2$ )	2.714	5.756	2.760	2.713

Table VI. Calculated solidus temperature using the Lever rule and simple model for steels S1, S2 and S3 (Table III conditions).

Sample	0.044wt%C		0.18wt%C		0.8wt%C	
	Lever rule	Simple model	Lever rule	Simple model	Lever rule	Simple model
S1	1510.28 ( $^{\circ}\text{C}$ )	1509.04	1486.78	1484.88	1344.55	1340.31
S2	1502.55	1499.90	1473.63	1465.28	1331.39	1314.14
S3	1491.59	1487.86	1460.73	1447.13	1318.49	1287.40

Table VII. Calculated secondary dendrite arm spacings from Eq. (12) for steel S3 (Table III).

$C_R$ ( $^{\circ}\text{C}/\text{sec}$ )	$\lambda_{\text{SDAS}}$ ( $\mu\text{m}$ )		
	0.044wt%C	0.18wt%C	0.8wt%C
1	137.4	103.7	182.0
10	44.1	45.1	79.0
100	14.2	19.6	34.4

Table VIII. Calculated solidus temperatures using the simple model for steel S3 (Table III).

$C_R$ ( $^{\circ}\text{C}/\text{sec}$ )	0.044wt%C		0.18wt%C		0.8wt%C	
	$\lambda_{\text{SDAS}}$ ( $\mu\text{m}$ )	$T_{\text{sol}}$ ( $^{\circ}\text{C}$ )	$\lambda_{\text{SDAS}}$	$T_{\text{sol}}$	$\lambda_{\text{SDAS}}$	$T_{\text{sol}}$
1. Constant secondary dendrite arm spacing						
1	44.1	1491.00	45.1	1455.64	79.0	1308.44
10	44.1	1487.86	45.1	1447.13	79.0	1287.40
100	44.1	1478.39	45.1	1428.13	79.0	1234.14
2. Constant cooling rate						
10	137.4	1478.55	130.7	1434.06	182.0	1254.72
10	44.1	1487.86	45.1	1447.13	79.0	1287.40
10	14.2	1490.99	19.6	1454.00	34.4	1304.75
3. Combined effects of cooling rate and secondary dendrite arm spacing						
1	137.4	1487.93	130.7	1450.38	182.0	1295.43
10	44.1	1487.86	45.1	1447.13	79.0	1287.40
100	14.2	1487.78	19.6	1442.83	34.4	1277.52

## FIGURE LIST

Figure 1 Comparison of the predicted and measured secondary dendrite arm spacings[47-51] as a function of carbon content at various cooling rates.

Figure 2 (a) Schematic of the dendrite array morphology and (b) the corresponding transverse cross section assumed in the finite difference simulation.

Figure 3 Numerical discretization of dendrite section for finite difference model domain.

Figure 4 Eutectic fraction (Al-4.9%Cu alloy in Table 2) predicted with the simple model compared with experimental measurements[21] and the numerical prediction by Voller *et al.*[8].

Figure 5 Comparison of manganese concentration in the liquid calculated by various simple equations with the present finite difference model results (0.13%C steel M1 in Table 3).

Figure 6 Comparison of carbon concentration in the liquid calculated by various simple equations with the present finite difference model results (0.13%C steel M1 in Table 3).

Figure 7 Comparison of the calculated (a) manganese and (b) phosphorus concentration in the liquid phase and experimental measurements[17] (0.13%C steel M1 in Table 3).

Figure 8 Non-equilibrium pseudo-binary Fe-C phase diagram of 0.015Si-1.05Mn-0.0009P-0.0008S carbon steels at a cooling rate of 0.17 °C/sec, compared with ZST and ZDT measurements[22].

Figure 9 Non-equilibrium pseudo-binary Fe-C phase diagram of 0.24Si-0.61Mn-0.015P-0.009S carbon steels at a cooling rate of 1 °C/sec, compared with ZST and ZDT measurements[23].

Figure 10 Non-equilibrium pseudo-binary Fe-C phase diagram of 0.34Si-1.52Mn-0.012P-0.015S carbon steels at a cooling rate of 10 °C/sec, compared with ZST and ZDT measurements[24].

Figure 11 Calculated *vs* experimental liquidus[27-30], solidus[27-30], peritectic temperatures [27-29], ZST[22-24,26] and ZDT[22-26] in plain carbon steels.

Figure 12 Effect of cooling rate on phase fraction evolution for three different steels calculated with simple model.

Figure 13 Effect of secondary dendrite arm spacing on phase fraction evolution for three different steels calculated with simple model.

Figure 14 Evolution of phase fractions with temperature during solidification for conditions in Table 6 calculated with (a) simple model and (b) finite difference model.

Figure 15 Combined effects of cooling rate and secondary dendrite arm spacing (Eq. 12) on  $T_{liq}$  ( $f_s=0.0$ ), ZST ( $f_s=0.75$ ), LIT ( $f_s=0.9$ ) and ZDT ( $f_s=1.0$ ) of steel S3 (in Table 3) calculated with simple microsegregation model.

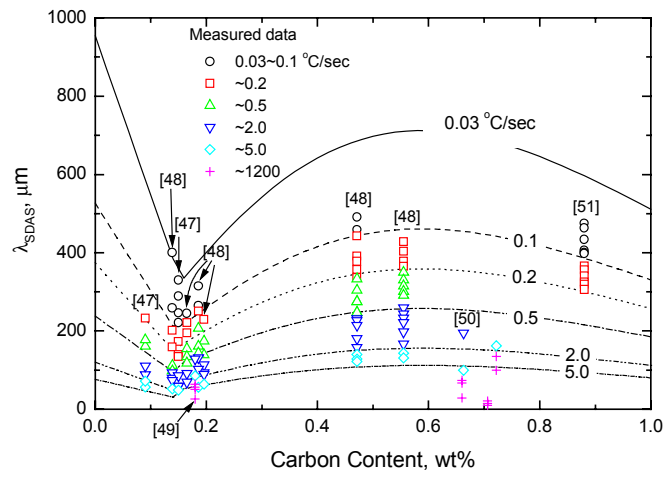


Figure 1 Comparison of the predicted and measured secondary dendrite arm spacings[47-51] as a function of carbon content at various cooling rates.

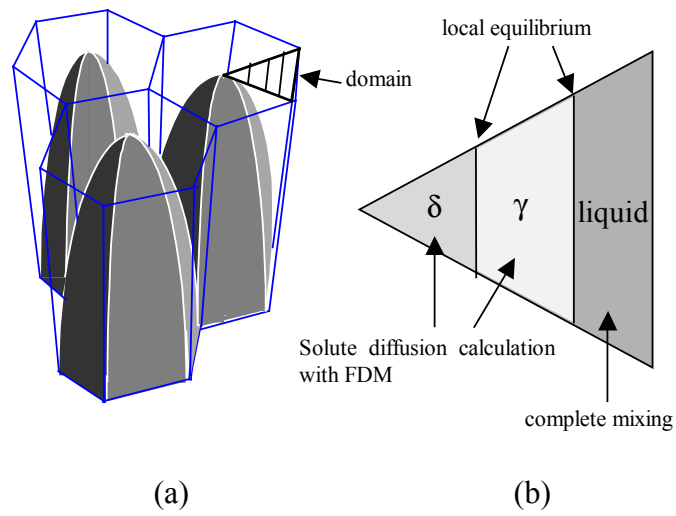


Figure 2 (a) Schematic of the dendrite array morphology and (b) the corresponding transverse cross section assumed in the finite difference simulation.

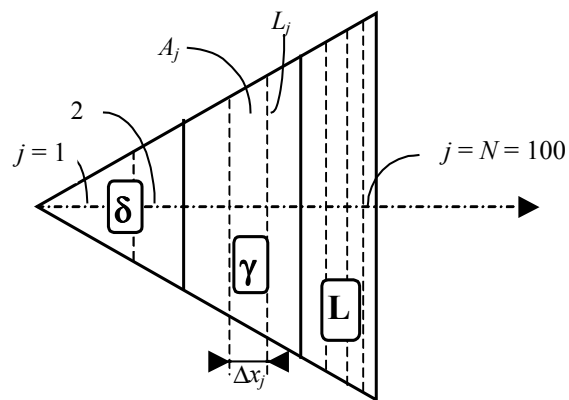


Figure 3 Numerical discretization of dendrite section for finite difference model domain.

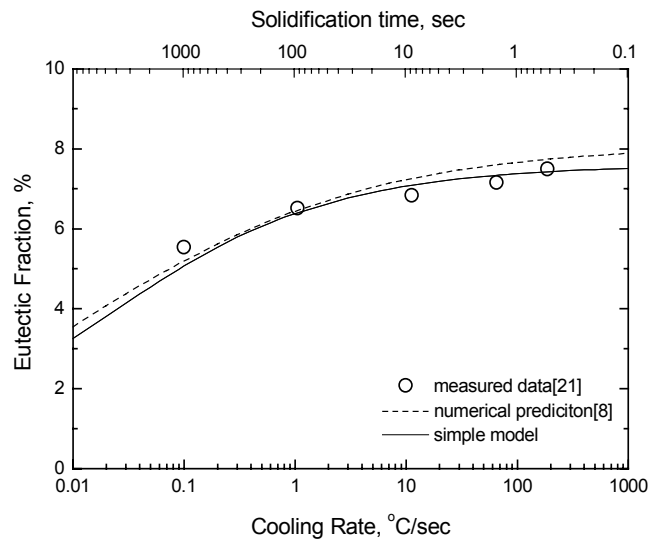


Figure 4 Eutectic fraction (Al-4.9%Cu alloy in Table 2) predicted with the simple model compared with experimental measurements[21] and the numerical prediction by Voller *et al.*[8].



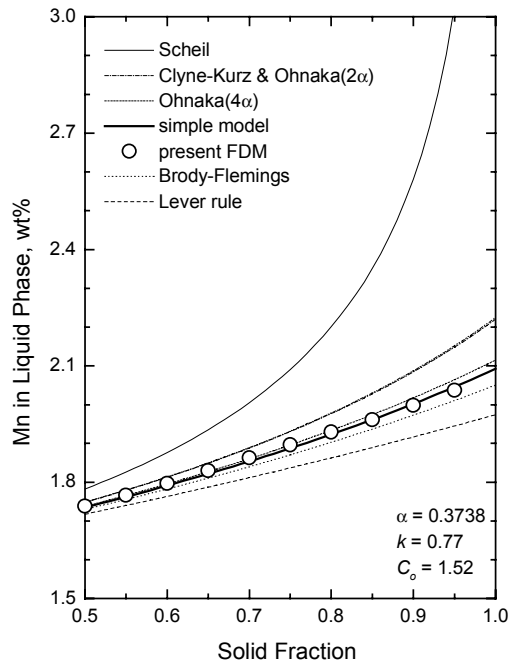


Figure 5 Comparison of manganese concentration in the liquid calculated by various simple equations with the present finite difference model results (0.13%C steel M1 in Table 3).

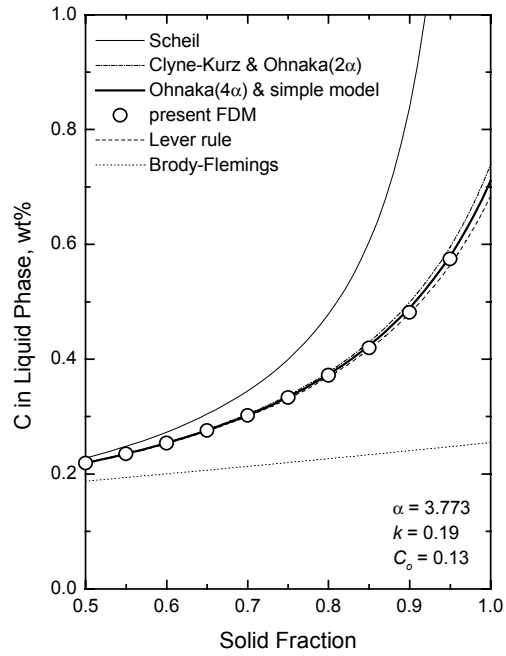
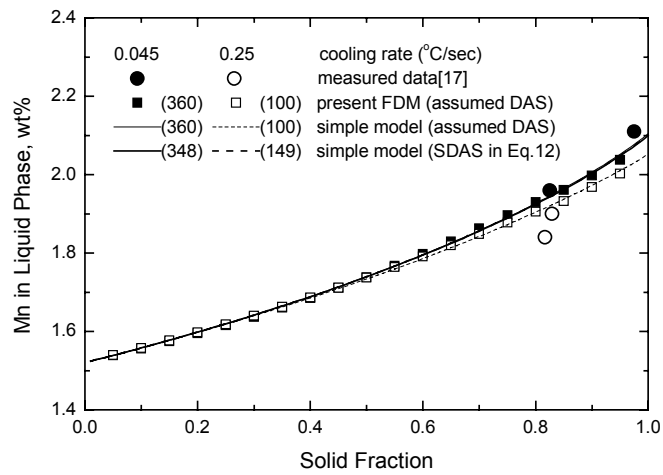
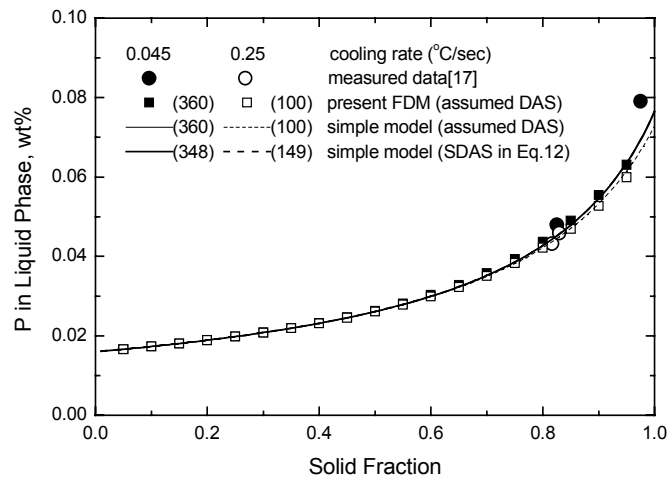


Figure 6 Comparison of carbon concentration in the liquid calculated by various simple equations with the present finite difference model results (0.13%C steel M1 in Table 3).



(a)

Figure 7 Comparison of the calculated (a) manganese and (b) phosphorus concentration in the liquid phase and experimental measurements[17] (0.13%C steel M1 in Table 3).



(b)

Figure 7 Comparison of the calculated (a) manganese and (b) phosphorus concentration in the liquid phase and experimental measurements[17] (0.13%C steel M1 in Table 3).

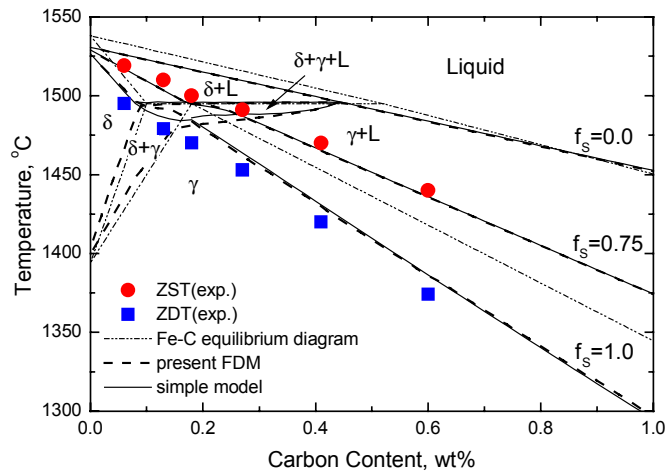


Figure 8 Non-equilibrium pseudo-binary Fe-C phase diagram of 0.015Si-1.05Mn-0.0009P-0.0008S carbon steels at a cooling rate of 0.17 °C/sec, compared with ZST and ZDT measurements[22].

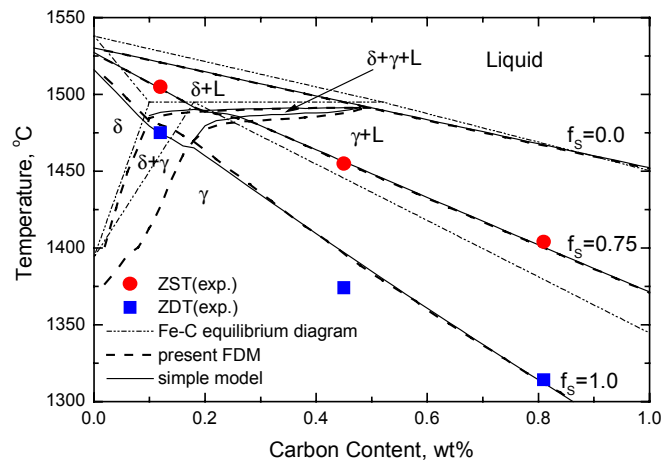


Figure 9 Non-equilibrium pseudo-binary Fe-C phase diagram of 0.24Si-0.61Mn-0.015P-0.009S carbon steels at a cooling rate of 1 °C/sec, compared with ZST and ZDT measurements[23].

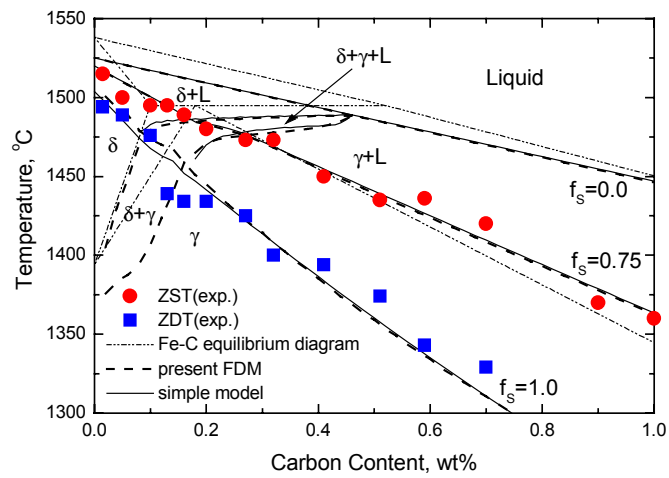


Figure 10 Non-equilibrium pseudo-binary Fe-C phase diagram of 0.34Si-1.52Mn-0.012P-0.015S carbon steels at a cooling rate of 10 °C/sec, compared with ZST and ZDT measurements[24].

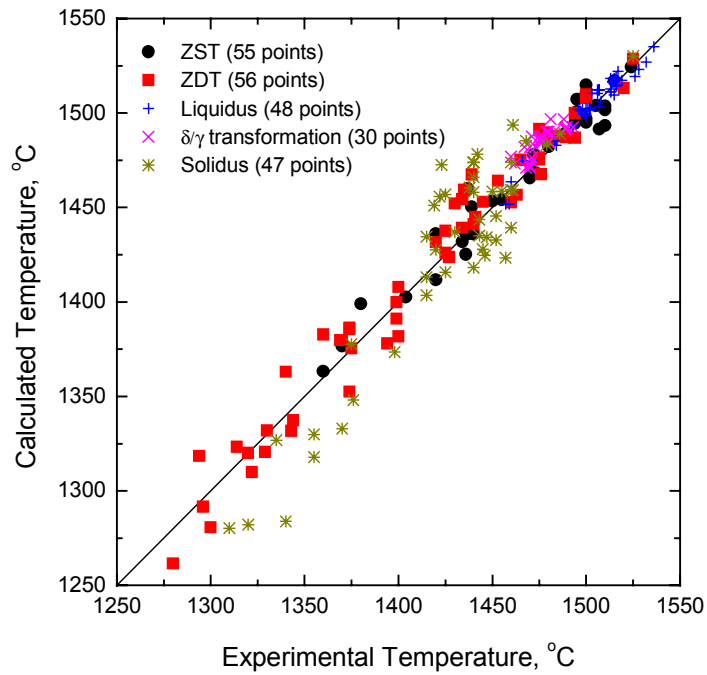


Figure 11 Calculated vs experimental liquidus[27-30], solidus[27-30], peritectic temperatures[27-29], ZST[22-24,26] and ZDT[22-26] in plain carbon steels.



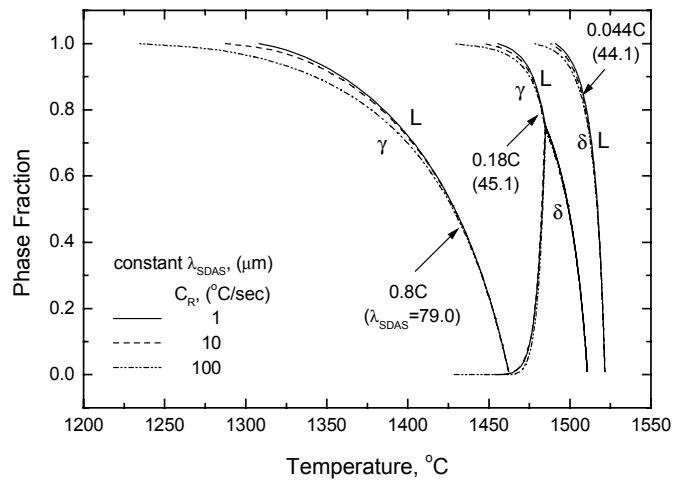


Figure 12 Effect of cooling rate on phase fraction evolution for three different steels calculated with simple model.

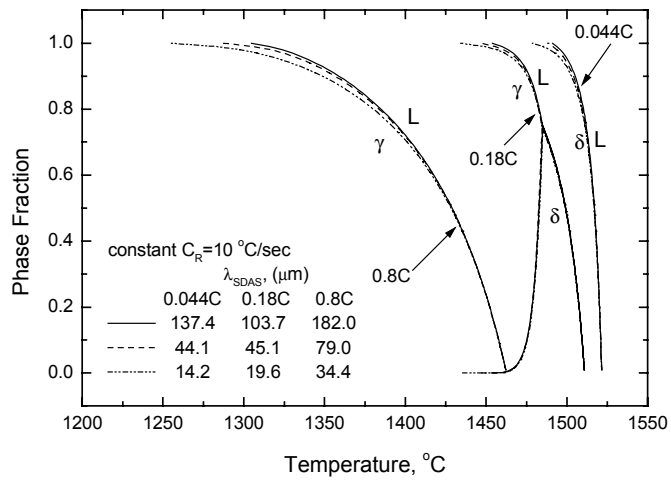
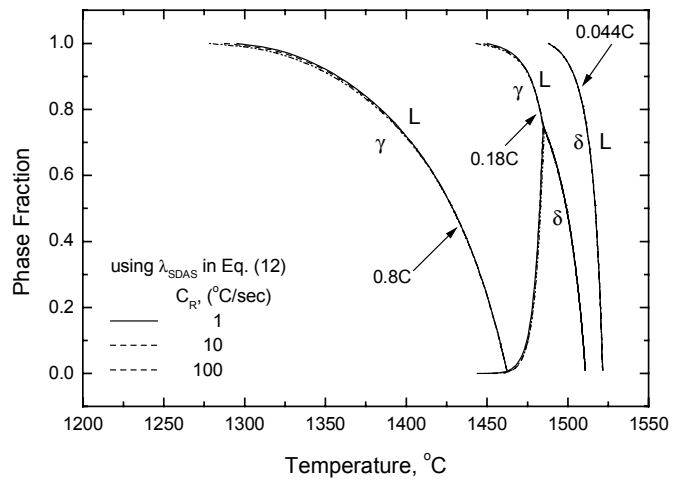
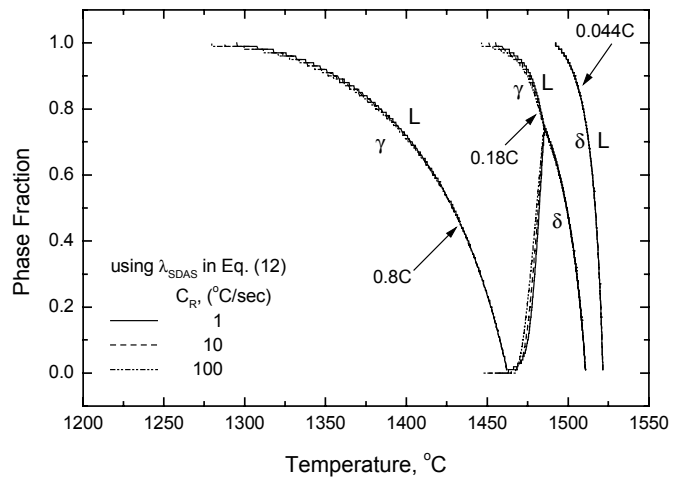


Figure 13 Effect of secondary dendrite arm spacing on phase fraction evolution for three different steels calculated with simple model.



(a)

Figure 14 Evolution of phase fractions with temperature during solidification for conditions in Table 6 calculated with (a) simple model and (b) finite difference model.



(b)

Figure 14 Evolution of phase fractions with temperature during solidification for conditions in Table 6 calculated with (a) simple model and (b) finite difference model.

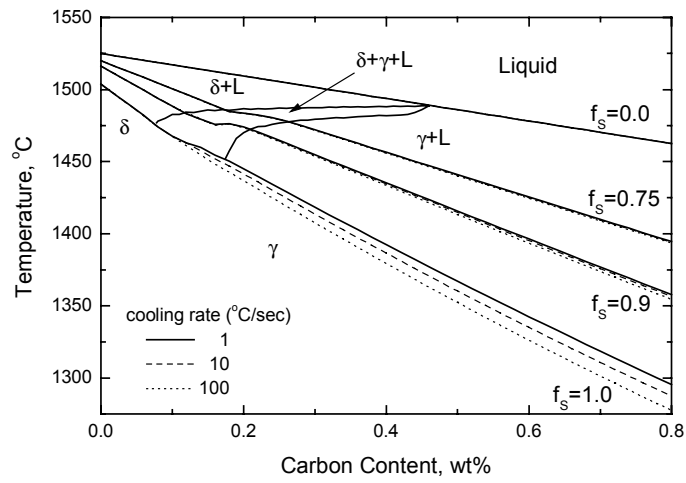


Figure 15 Combined effects of cooling rate and secondary dendrite arm spacing (Eq. 12) on  $T_{liq}$  ( $f_s=0.0$ ), ZST ( $f_s=0.75$ ), LIT ( $f_s=0.9$ ) and ZDT ( $f_s=1.0$ ) of steel S3 (in Table 3) calculated with simple microsegregation model.